Radiation risk and image quality assessment of Digital Variance Angiography
In-vivo multimodal preclinical imaging

Ph.D. thesis

Richard Elek

Theoretical and Translational Medicine Division
Semmelweis University

Supervisor: Szabolcs Osváth, Ph.D.

Official reviewers: Szabolcs Czifrus, Ph.D.

Károly Liliom, Ph.D.

Head of the Complex Examination Committee:

György Reusz, MD, Ph.D., D.Sc.

Members of the Final Examination Committee:

Orsolya Kiss, Ph.D.

Ákos Jobbágy, Ph.D.

Budapest, 2026

1 Introduction

Interventional radiology (IR) is a medical specialty that uses imaging to facilitate the introduction and guidance of devices into the body. Digital Subtraction Angiography (DSA) is the traditional image processing method for contrast agents. Digital Variance Angiography (DVA) uses a different, but more efficient image processing technique. (Fig. 1).

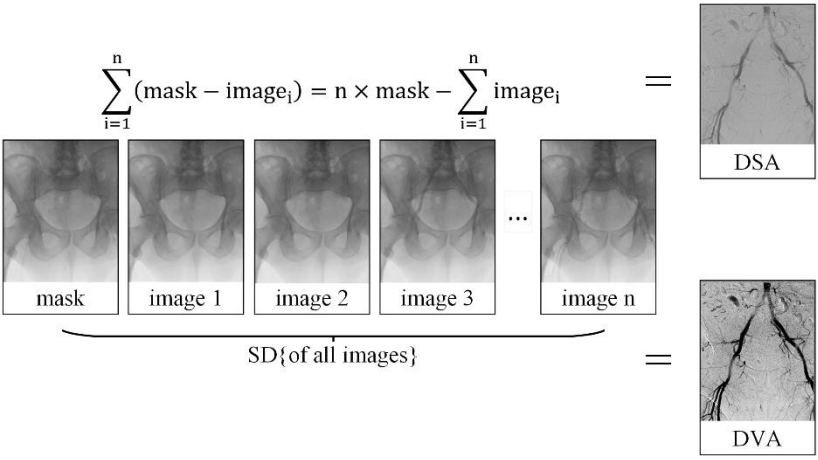

Fig. 1. In Digital Subtraction Angiography (DSA, top), the first image of the series is typically used as a mask, and it is subtracted from all subsequent images to highlight contrast-enhanced structures. These could be then summed as here or merged in another way. On the contrary, Digital Variance Angiography (DVA, bottom) processes the entire image series to enhance the visibility of vascular structures by leveraging temporal statistical properties (i.e., the standard deviation or SD). This figure illustrates the image processing principles of DSA and DVA and shows their respective outputs.

This work aims to assess the impact of DVA in terms of effective dose and other associated radiological risk metrics, lifetime attributable risks of cancer incidence and mortality. Another

question addressed in this thesis is the objective evaluation of image quality to support the clinical commissioning of the Kinepict Medical Imaging Tool (KMIT) in IR suites and to quantitatively demonstrate its benefits using an image quality test object (IQTO).
Overall, this thesis presents a comprehensive evaluation of DVA technology, integrating both radiation dose and risk assessment with objective image quality analysis, thereby providing a quantitative demonstration of its clinical benefits.

2 Objectives

In order to estimate radiation risks, one must set a model to calculate organ absorbed doses by the means of Monte Carlo simulations (MC), then estimate effective dose and lifetime attributable risk (LAR). For the goals we set, we had to develop a new IQTO. Brief summary of goals:

1. Further validation of dosimetric quantities to provide a solid basis for our studies.
2. Development of a particle transport simulation framework based on a generic, validated MC simulation software suite.
3. Estimate risks from clinical studies and analyse data to provide evidence for the efficacy of DVA.
4. Develop a test device (IQTO) and establish a methodology for the objective evaluation of DVA image quality enhancement.

3 Methods

The methods section is based on the publications related to the present work. Both publications are published under the CC BY 4.0 terms: https://creativecommons.org/licenses/by/4.0/
Both clinical studies referenced in this work have undergone ethical approval by the Hungarian National Institute of Pharmacy and Nutrition, reference number OGYÉI/2830/2017 (NCT04343196) and the Institutional Review Board of the

Frankfurt University Hospital (ref. 2022-941). All studies were in accordance with the 1964 Helsinki Declaration. Written informed consent was obtained from all participants included in the study.

3.1 Validation of dosimetric quantities

The Siemens Artis Zee Floor machine at the Heart and Vascular Centre of Semmelweis University and the GE Innova IGS 540 unit at the Semmelweis University Medical Imaging Centre were checked for the accuracy of incident air kerma (IAK) and entrance surface air kerma (ESAK) (Fig. 2) indices with a PTW UNIDOS Webline electrometer and a legally verified 30013 Farmer-type ionisation chamber. RTI Piranha 657 X-ray multi-meter was used to test the half-value layer and total filtration. At least 40 frames were used for each setting. The prostatic artery embolisation (PAE) study was conducted on a Siemens Artis pheno at the Frankfurt University Hospital. This device is under a quality assurance program.

Fig. 2. Geometrical set-up for the measurement of ESAK (left, includes backscatter) and IAK (right, without backscatter) which were used to determine the accuracy of displayed dose indices.

3.2 Risk assessment of angiographic procedures

Only stationary acquisitions (SA) were used for the comparison between DSA and DVA. The Digital Imaging and Communications in Medicine (DICOM, or DCM) files exported from the angiographic units were used to acquire information for the MC simulations (Fig. 3). Python (v3.9) was selected as the implementation language for the framework. The accuracy of the extracted data was double-checked manually with OFFIS DCMTK, ImageJ and MicroDICOM.

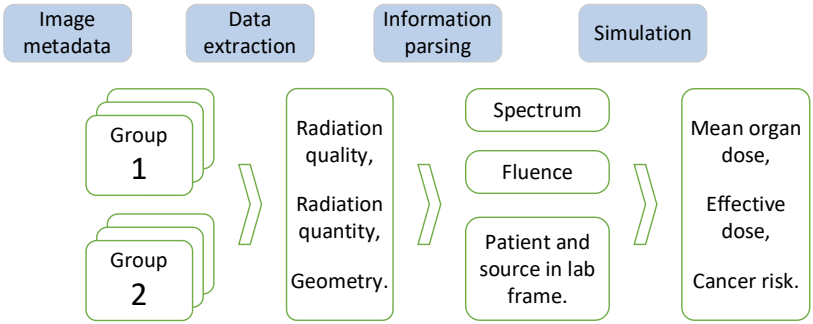

Fig. 3. The workflow of the particle transport framework. Group 1 and group 2 denotes the DVA and DSA groups for the study on PAD procedures and it denotes the normal dose (ND) and ultra-low dose (ULD) groups for the PAE procedures' study. First, a DICOM image series data export is necessary using the metadata of the headers. Then the algorithm extracts the data for each irradiation event and their corresponding exposure parameters. Patient related data are supplied externally (age, height, weight). Based on the parsed data, particle fluence and energy distribution are determined along with the definition for the geometry of the irradiation event. After running the simulations, risk related metrics (ED and LAR) are calculated based on the organ absorbed doses determined by the MC simulations.

The next table (Table 1) summarises the DICOM tags and their corresponding identifiers used in the framework.

Table 1. DICOM data tags extracted from image series.

Identification	Image unique identifier (UID) (0008,0018); patient name (0010,0010, as 'patient_X')
Patient-related data	Patient age (0010,1010), patient sex (0010,0040);
Radiation quality	kVp (0018,0060); added filtration (0021,100a);
Radiation quantity	Kerma-area product (0018,115e);
Irradiation geometry-related information	Patient position (0018,5100); Source to image receptor distance (0018,1110); Primary angle (0018,1510); Secondary angle (0018,1511); Table position (0021,1057) as Lat.\Long.\Height coordinates*; Shutter and collimator related data (0018, 1600; 1602; 1604; 1606; 1608 and 0018,1700; 1702; 1704; 1706; 1708), including pixel spacing (0018, 1164) to calculate the field size.
Auxiliary information	Patient height and weight. These were available separately as no DICOM tags encoded this information.

* Determined experimentally

3.2.1 Data collection for PAD procedures

Building on the study by Sótonyi et al. on Peripheral Artery Disease (PAD) diagnostic procedures, we initially extracted exposure data for all patients. The exposure and the Radiation Dose Structured Report (RDSR) data was reviewed. Ultimately 54 patients underwent PAD using DVA, while 53 underwent the procedure with traditional DSA.

3.2.2 Data collection for PAE procedures

In the normal dose (ND) group 35 patients undergone the PAE with the CARE aorta and CARE pelvis protocol, while the ultra-low ULD group (35 patients) had a target dose level reduced to 28%. Procedural aspects were unchanged. DCM data were obtained from the RDSR files.

3.2.3 Qualification of the source

PENELOPE version 2018 was used to simulate particle transport. I have determined that the total filtration is at least 2.8 mm Al equivalent without additional filtration. SpekPy was used to generate the corresponding X-ray spectra at 1 keV bins. The X-ray source was considered to be a simple point source, where the inhomogeneity of the X-ray field due to the heel-effect, extra-focal radiation and the penumbra are neglected.

3.2.4 Quantification of the source

Another key aspect of the source term is the number of quanta emitted during an irradiation event. The number of quanta, *N*, was calculated using the following formula (eq. (1)):

$$N = \frac{KAP \times \rho_{air}}{\sum_n p_n E_n \mu_{en,n}} \quad (1)$$

where ρ_{air} [g/cm^3] is the density of air under standard conditions at sea level. The denominator describes the total energy fluence [J] from the spectrum as ($p_n E_n$) multiplied by the linear energy absorption coefficient, $\mu_{en,n}$ [1/cm] in the *n* bins.

3.2.5 Settings for the simulations

Fig. 4 illustrates the geometrical arrangement modelled for the simulated irradiations. The isocentre determines the central axis of the projection. This point serves as a reference to calculate the source position. Angiographic systems describe the beam using an isocentre-based coordinate system as referenced in Fig. 4.

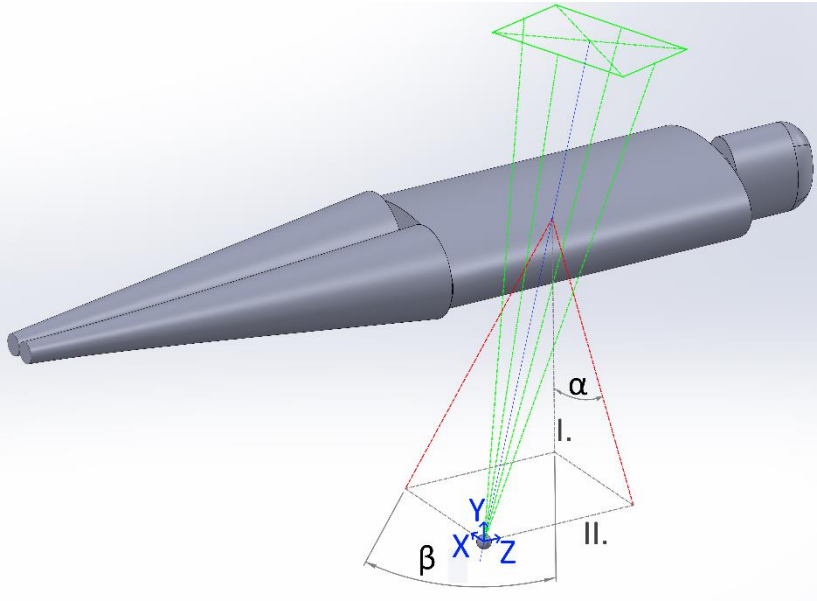

Fig. 4. Illustration of the anthropomorphic phantom lying on its back. The grey sphere at the bottom of the image represents the X-ray source. The thin blue line connecting the centre of the image plane with the source indicates the main axis of the beam. The isocentre is the centre of rotation, incident on the X-ray beam's main axis. The isocentre's projection is a vertical grey line (I.) perpendicular to the laboratory reference frame's X-Z plane (II.). Position of the C-arm is determined by the primary and secondary angles measured from the isocentre's vertical projection. The lowercase Greek letters α and β denote the primary and secondary angles, respectively. The green lines at the image plane illustrate the rectangular radiation field. The operating table and the mattress below the patient were taken into account in the simulations, but are not shown in this figure for the sake of discernibility.

Simple trigonometric calculation was used thereon. Quadric geometry adult mathematical phantoms were used, both male and female patients. These are based on the adult-type phantom, excluding organs that are not present for the corresponding sex (breast, uterus and ovaries for males; prostate and testes for females). Rescaling was also applied to fit the actual patient habitus, according to (eq. (2)) for height (h), in direction Z:

$$s_z = \frac{h}{h_0} \tag{2}$$

where s_z is the scaling factor and h_0 is the phantom's height (178.5 cm). To account for the patient's weight M, the phantom in the X-Y direction can be changed using the following scaling factor, s_{xy} (eq. (3)):

$$s_{xy} = \sqrt{\frac{h_0\, M}{h\, M_0}} \tag{3}$$

where M_0 is the phantom's unscaled weight. Eq. (4) describes the scaling factors for the phantom:

$$x = s_{xy} x_o \qquad y = s_{xy} y_o \qquad z = s_z z_o \tag{4}$$

The patient support was modelled as a homogenous body of carbon fibre and epoxy (0.713% H, 96.022% C, 2.262% O, 1.003% Cl; 1.79 g/cm^3). Organs correspond to ICRP 103.

Each simulation was initiated with 1 million showers to provide reliable statistics but a relatively low computing time of 15 minutes. This allowed the statistical uncertainty of each simulation to stay below 5% for all organs in the beam. Electron and photon cut-off energies are the default (1/100th of the maximum) and no variance reduction techniques were used.

3.2.6 Organ dose and cancer risk estimation

The absorbed dose of each organ was calculated and weighted by the tissue weighting factors recommended by the International Commission on Radiation Protection (ICRP 103 publication). The absorbed dose of an organ (D_{organ}) is calculated according to the following equation (eq. (5)).

$$D_{organ} = Nk\frac{\sum \bar{E}_{body,organ}}{M_{organ}} \quad (5)$$

where $\bar{E}_{body,organ}$ is the average energy absorbed in each body (eV). The total mass of the organ is M_{organ} in kg. N is the number of photons obtained from equation (1). The factor k is $1.602176565\times10^{-19}$ J/eV.

For the active (red) bone marrow, the average absorbed energy in the bone was multiplied by 1.12 (peak of the attenuation coefficients' ratio) and the ratio for red/yellow bone marrow was accounted for. To estimate the absorbed dose to the lymph nodes, selected organs' average absorbed dose was weighted and summed. The effective dose (here: E) was calculated according to the recommendations of the ICRP 103, using the following equation (eq. (6)):

$$E = \sum_{T} w_T D_{organ} \quad (6)$$

where the radiation weighting factor is omitted as its value is 1 for photon radiations and w_T denotes the tissue weighting factors from ICRP 103.

LAR was calculated for both cancer incidence and mortality. The basis for these is the "BEIR VII" report We assumed that the expected lifetime (attainable age) of Hungarians does not differ significantly from the one determined for the population of the United States of America.

3.3 Comparative assessment of DVA and DSA

The two groups were compared based on each patient's total, FLU and SA KAP, along with the charge, current, pulse width, tube voltage, added filtration, field size, total number of frames for each type of image acquisition, age, weight and body mass index. Any bias between the two groups would mean that they were treated or selected differently. The Mann-Whitney U-test was used to find out if there is a significant difference between these indicators. The statistical data were processed with JASP (v0.18.3) and Orange Data Mining (v3.38).

3.3.1 PAD procedures' evaluation

The PAD diagnostic procedure for the DVA group used a reduced dose protocol, while DSA group had the regular one.

3.3.2 PAE procedures' evaluation

The Fisher's exact test was used to test differences in patient characteristics, while the Mann-Whitney U-test was used to test bias in procedural aspects of the PAE procedures. Different statistical tests were utilised to evaluate the Likert scale scores of raters for DSA and DVA image pairs. The categories of evaluation were the visualisation of large vessels, small vessels, tissue blush and noise. Likert scale for diagnostic image quality: (1) non-diagnostic; (2) poor; (3) average; (4) good; and (5) excellent. Additionally, artifacts were evaluated on a similar five-point Likert scale: (1) severe; (2) noticeable; (3) moderate; (4) minimal; (5) no visible. An additional option was available, if the structure was not present (for some cases of tissue blush). DSA and DVA were compared within the same patient group to quantify the potential image enhancement achieved by DVA. ND-DSA was compared with ULD-DVA. The former analysis employed one-sample statistical methods, whereas the latter required two-sample approaches. High interrater agreement is essential. For within-sample interrater comparisons Kendall's Tau-b, whereas Bangdiwala's B statistic was used for the two-sample agreement between raters. The ND-DSA and ULD-DVA protocols were also compared by the average and standard error of the ratings. The significance of the results was assessed with the Mann-Whitney U-test. A rater-pairwise Spearman correlation test was employed to demonstrate consistency of ratings. A simple statistical evaluation was done by comparing scores from the raters.

3.4 Objective image quality assessment

A test device with a rotating insert was developed. Differing thicknesses of aluminium plates (0.05, 0.1, 0.2 and 0.4 mm) and a copper-plate set on the stationary part (0.2 to 1.4 mm in 0.2 mm steps) are featured. This IQTO is non-binary and enables the evaluation of an image series. An image of the test device is shown below (Fig. 5).

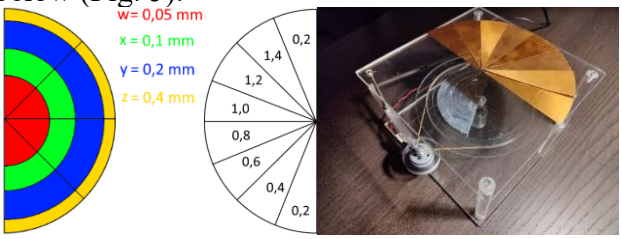

Fig. 5. Test device with a rotating insert. From left to right: Colour illustration of the aluminium filters and their thickness on the rotating plate; Illustration of the copper plates on top of the test device, divided into sectors, showing the thickness of each copper sector in mm units (decimal separator: ","); Photograph of the test device.

The GE X-ray unit was used to image the IQTO under different circumstances. Different dose settings (100% and 50% target dose rate modes), frame generation frequency (0,5; 1; 2; 4; 7,5 fps), 4 different settings for the rotation speed of the insert (approximately 128, 100, 56 and 40 rpm) corresponding to blood flow rate; and either 2 consecutive images, image series from 1 rotation or exactly 10 consecutive images were evaluated. Each image series underwent the calculation of the summed DSA image (Fig. 1) and calculation by the KMIT software tool (v5.0.3.856). The single DSA and DVA images were evaluated using ImageJ. Contrast to noise ratio (CNR) was chosen as the singular figure of merit. The CNR was calculated according to eq. (7):

$$CNR = \left| \frac{MPV_x - MPV_{bkgx}}{\sqrt{SD_x^2 + SD_{bkgx}^2}} \right| \quad (7)$$

where *MPV* is the mean pixel value, *SD* is their standard deviation and *x* denotes a given sector's section, while *bkgx* refers to the corresponding sector's outmost area on the IQTO (Fig. 6).

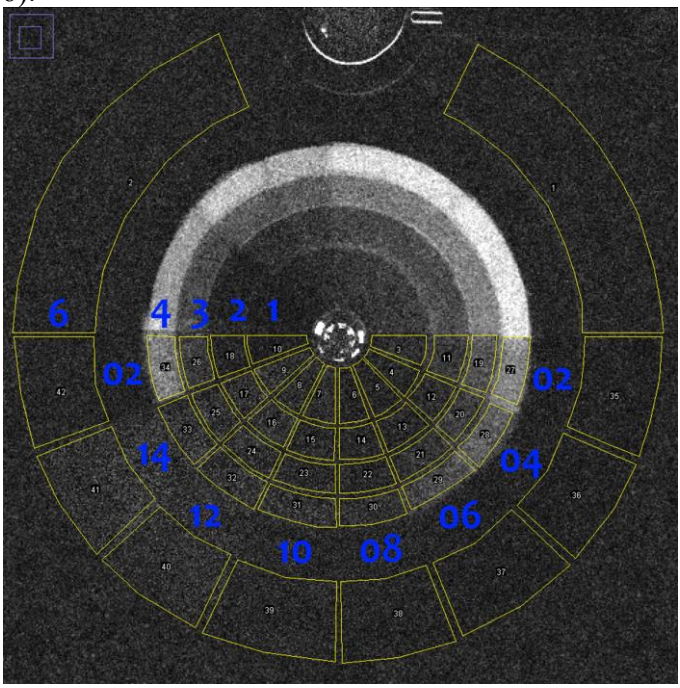

Fig. 6. An X-ray image of the rotating test device, showing the different ROIs. Notations 02…14 in the circular pattern show the thickness of the stationary copper plates' sectors in 0.1 mm units. Copper plates extend beyond the outmost ROIs. Notation 6 shows the outmost stationary copper plates' section. Notations 1 through 4 denote the innermost (0.05 mm aluminium) and the outmost (0.4 mm aluminium) sections of the circular aluminium plate. The drive may be seen on top of the image.

4 Results

4.1 Validation of dosimetric quantities

The efforts for the verification of the displayed KAP resulted in satisfactory results.

4.2 Risk assessment of angiographic procedures

4.2.1 PAD procedures' risk assessment

The group which was examined with DSA received a collective effective dose of 194.7 man×mSv, while the other one for which DVA was utilised, has received 42% of this, 82.6 man×mSv. The collective effective dose in the DVA group has been reduced by 58% in this study. The range of cancer incidence (by 25…75%) and cancer mortality reduction (51…84%) varied slightly.

4.2.2 PAE procedures' risk assessment

The ND group which was examined with DSA received a collective effective dose of 229.8 man×mSv, while the ULD group has received 21.5% of this, 49.3 man×mSv. The collective effective dose in the DVA group has been reduced by 78.5%. Cancer incidence was reduced by 71…92%, while cancer mortality was reduced by 71…91%.

4.3 Comparative assessment of DVA and DSA

4.3.1 PAD procedures' risk assessment

In the PAD study, the DSA group had 53 (36 male), while the DVA group had 54 (44 male) patients. Our statistical analysis revealed that there was no bias among the two patient groups.
There was a significant difference in the SA's median KAP for DSA (4.76×10^{-4} Gym^2) and DVA (1.91×10^{-4} Gym^2).

4.3.2 PAE procedures' evaluation

The mean cumulative KAP from SA was reduced by 80% among the ND and ULD groups. No procedural or differences in patient characteristics were observed.

According to the Bangdiwala's B evaluation, raters A, B, and C agreed that ND-DVA and ULD-DVA provided better visualization of large and small vessels, as well as tissue blush. For background noise, the results varied ($p = 0.047$ for rater A, 0.002 for B, and 0.085 for C). The Spearman test showed a strong correlation in all pairwise comparisons of raters' evaluations of large and small vessels and tissue blush ($p < 0.001$) for both ND and ULD acquisitions. However, no correlation was found for background noise ratings between raters A and B ($p = 0.643$) or A and C ($p = 0.166$) in ND images, while a moderate correlation was observed between raters B and C ($p = 0.033$). For ULD images, background noise ratings showed strong correlations across all rater comparisons ($p < 0.001$ for A-B, $p = 0.015$ for A-C, and $p = 0.015$ for B-C). For both ND and ULD ratings, raters showed strong agreement on large and small vessels and tissue blush ($p < 0.001$). For background noise in the ND-DSA dataset, disagreement was observed ($p = 0.640$ for rater A-B, 0.161 for A-C, and 0.036 for B-C). In contrast, ULD-DVA ratings showed strong agreement between raters A and B ($p < 0.001$), with slight disagreement between A-C and B-C (both $p = 0.016$).

For large vessels, the mean score for ND-DVA (2.94 ± 0.14) was significantly higher than ND-DSA (1.94 ± 0.088), while ULD-DVA (3.033 ± 0.136) also exceeded ULD-DSA (2.00 ± 0.10). Similar trends were observed for small vessels, where ND-DVA (3.98 ± 0.10) and ULD-DVA (4.11 ± 0.09) achieved notably higher scores compared to ND-DSA (2.88 ± 0.08) and ULD-DSA (3.03 ± 0.08) ($p < 0.001$). Tissue blush also demonstrated a marked difference, with ND-DVA (2.41 ± 0.12) and ULD-DVA (2.79 ± 0.10) scored significantly better than ND-DSA (1.58 ± 0.08) and ULD-DSA (1.84 ± 0.08) ($p < 0.001$). For background noise, DVA also outperformed DSA. A summary of rater preference may be found below.

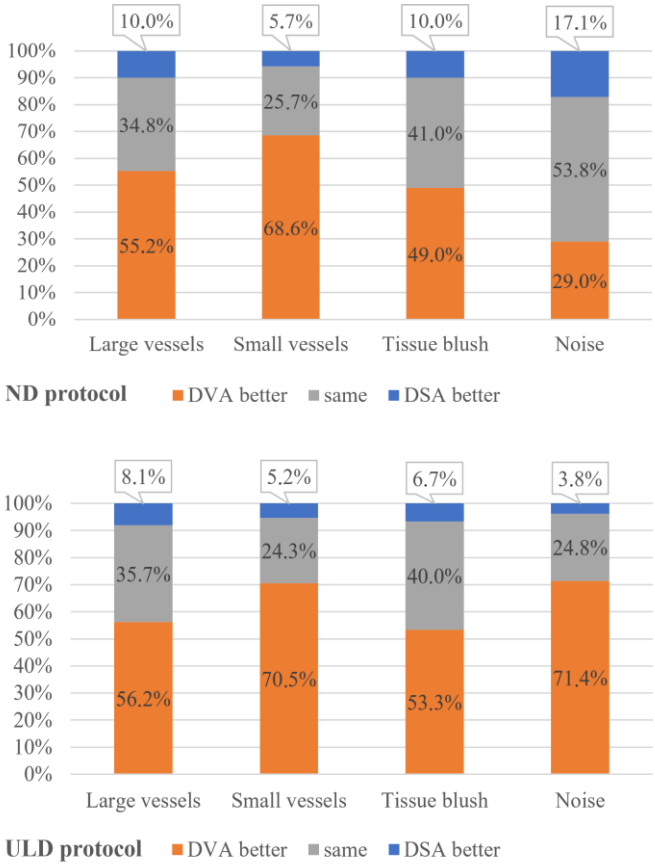

Fig. 7. Stacked column charts illustrating the qualitative preference of the 3 raters for image quality across four evaluation categories: large vessels, small vessels, tissue blush, and background noise. The plot compares the qualitative preference of each rater between the imaging datasets from normal dose (ND, upper panel) and ultra-low dose (ULD, bottom panel) imaging protocols with DVA (orange) and DSA (blue) image processing. Instances where no difference was observed are labelled as "same" with grey colour.

4.4 Objective image quality assessment

The image quality phantom was evaluated by comparing pairs for all of the 10.800 settings. Where more than two images were used for the DVA and DSA image generation, the CNR was observed to be higher by up to a factor of 3.

5 Conclusions

DVA enables up to 80% reduction for SA in radiation exposure in complex interventional procedures. While reducing radiation dose, image quality is preserved.

The reduction of physical dose indices translates into the reduction of associated stochastic and deterministic radiation risks. Dose reduction of the patient draws along the reduction of dose to the staff and costs associated with care, benefiting patient outcome and contribute to sustainability. DVA is a valuable tool to help optimising radiation protection of patients and staff alike and could herald a paradigm shift in angiographic imaging.

Future research should explore the utility of DVA in contrast media use and further validate its benefits in clinical settings and implications for vulnerable patient cohorts.

Novel, thesis-related findings

1) I have verified that the dose metrics provided by the angiography units are satisfactory.
2) I have developed a MC particle transport simulation framework which relies on the image metadata from the angiographic procedures.
3) I have demonstrated the utility of this particle transport framework for the risk assessment of PAD and PAE procedures.
   a. With the use of DVA, radiation dose during an exposure may be reduced by up to 80% compared to the otherwise clinically used DSA imaging.
   b. Reduction of the quantities describing physical dose to the patient translates into a decreased risk of cancer incidence by 25% to 75% and cancer mortality by 51% to 84% for PAD procedures depending on the cancer site.
   c. The dose reduction in PAE results in the reduction of 71% to 92% in cancer incidence and 71 to 91% reduction in cancer mortality depending on the cancer site.
4) DVA is superior compared to DSA in subjective and objective image quality evaluations.
   a. I have designed and built a test object to quantitatively evaluate the CNR of DVA and demonstrated that if more than two images are processed by KMIT, DVA has an advantage in terms of CNR compared to summed DSA, by up to a factor of 3.
   b. A randomized controlled trial for PAE revealed that DVA images are superior to DSA for the visualisation of large vessels, small vessels and tissue blush in subjective evaluations of PAE procedures, as DVA achieved significantly higher scores from experienced raters ($p < 0.001$; rating: 3.03 vs 2.00; 4.11 vs 2.88; 2.79 vs 1.58 respectively) under any target dose rates.

Bibliography of the candidate's publications
Publications related to the thesis:

1. Elek R, Herényi L, Gyánó M, Nemes B, Osváth S. Comparative effectiveness of digital variance and subtraction angiography in lower limb angiography: A Monte Carlo modelling approach. Phys Med. 2024;128:104859. doi:10.1016/j.ejmp.2024.104859

2. Alizadeh LS., Vogl TJ, Rafi W, Caruso M, Elek R, Osvath Sz, Nica A, Gruenewald LD, Yel I, Goekduman A, Koch V, Dimitrova M, D'Angelo T, Booz C. Digital variance angiography enables up to 80% reduction in stationary acquisition radiation dose during prostatic artery embolization: a prospective randomized trial. Eur. Radiol. 2026; doi: 10.1007/s00330-025-12235-3. Epub ahead of print.

∑IF: 7.4

Publications not related to the thesis:

1. Sudár Á, Pócza T, Elek R, Major T, Tárnoki ÁD, Tárnoki DL, Pesznyák C. Expansion of applicability of multiple scan average dose measurements for CT dosimetry. Phys Med Biol. 2025 Aug 12;70(16). doi: 10.1088/1361-6560/adf40d. PMID: 40706629.
2. Elek R, Osváth S. Evaluation of a novel imaging method of vessels and moving objects, digital variance angiography. 5th European Congress of Medical Physics, 2024.
3. Osváth S, Elek R. Honey I shrunk the dose! 5th European Congress of Medical Physics, 2024.

4. Kovács B, Szőnyi-Pákai R, Gáspár L, Elek R. A személyi dozimetria fejlesztése az Izotóp Intézet Kft.-nél, SUGÁRVÉDELEM, vol. XVII, no. 1, pp. 22–32, 2024.
5. Elek R, Mihályi D, Tóth N, Váradi C, Dankó Z., Balázs E, Sáfrány G, Bágyi P. A nemzeti páciensdózis-felmérő program jelenlegi helyzete, SUGÁRVÉDELEM, vol. XV., no. 1, pp. 1–11, 2022.
6. Kolozsi Z, Elek R, Pesznyák C. Sugárterhelést befolyásoló tényezők vizsgálata intervenciós radiológiai munkahelyeken, MAGYAR RADIOLÓGIA ONLINE, vol. 12, no. 6, pp. 1–12, 2021.
7. Elek R. Egyéni védőeszközök ellenőrzése röntgenmunkahelyeken, SUGÁRVÉDELEM, vol. XIV. évf. (2021), no. 1. szám, pp. 32–44, 2021.
8. Deme S, Elek R, Pesznyák C, Szűcs L. A pulzált neutronok dózisteljesítményének mérése, SUGÁRVÉDELEM, vol. XIV. (2021), no. 1, pp. 45–57, 2021.
9. Elek R, Várkonyi I, Kis É, Porubszky T. Újszülöttek és koraszülöttek röntgendiagnosztikai sugárterhelésének vizsgálata mellkasi, hasi és kombinált felvételek során, MAGYAR RADIOLÓGIA, vol. 89, no. 1, pp. 7–15, 2015.
10. Séra T, Porubszky T, Papos M, Elek R, Besenyi Z, Gion K, Bartha A, Pellet S, Pavics L. Validation of CT doses of SPECT/CT and PET/CT hybrid devices: lessons learned, NUCLEAR MEDICINE COMMUNICATIONS, vol. 35, no. 5, pp. 534–538, 2014.

∑IF: 5.1